JOURNAL OF PROPULSION AND POWER
Vol. 23, No. 1, January–February 2007

Finite Element Simulation of Blade Row Viscous Interactions: Vane Vibratory Stress Prediction

Kishore Ramakrishnan,* Patrick B. Lawless,† and Sanford Fleeter‡
Purdue University, West Lafayette, Indiana 47907

DOI: 10.2514/1.17187

A fluid-structure interaction analysis is developed to study wake-generated turbomachine blade row unsteady aerodynamics and to predict the resulting vibratory stress. This is accomplished by incorporating the Baldwin–Lomax turbulence model into TAM-ALE3D, a 3-D multimaterial finite element code employing an arbitrary Lagrangian Eulerian solver. This viscous TAM-ALE3D model is then utilized to simulate fluid-structure interactions in the Purdue Transonic Compressor. First, the viscous analysis is experimentally validated by simulating the rotor-stator interaction unsteady aerodynamics at the part-speed condition at which detailed experimental data are available. The resonant response of the stator vanes to the unsteady aerodynamic excitation is then predicted by performing a full fluid-structure interaction simulation.

Nomenclature

D_{ij}	=	deformation rate tensor
F^{hg}	=	hourglass viscous force
F_{Kleb}	=	Klebanoff intermittency function
F_{wake}	=	Baldwin–Lomax model function
M	=	mass of element/Mach number
P	=	isotropic part of stress tensor
q	=	shock smearing factor
S_{ij}	=	deviatoric stress tensor
U	=	mesh velocity
u	=	material velocity
$u_{i,j}$	=	velocity gradient tensor
V	=	volume
μ	=	(total) dynamic viscosity
ω	=	frequency/vorticity

Subscripts

e	=	elemental value
α	=	nodal value, node number

Introduction

BLADE failure due to high cycle fatigue (HCF) is a critical concern throughout the gas turbine industry, with HCF analysis a key technology development issue. To address this, simulation tools that model the multistage unsteady aerodynamic environment have been developed. Similarly, structural dynamic solvers are well advanced in their ability to predict the structural response of the blading. However, HCF is a coupled problem in which the unsteady aerodynamics affects the blade motion and vice versa, thereby requiring both the aerodynamics and structural dynamics to be dealt with simultaneously. Toward this end, capabilities to simulate the vibratory motion have been added/interfaced to unsteady Euler/Navier–Stokes solvers to calculate blade vibrations. However, the data transfer between the structural and fluid grids is time consuming and can often limit the accuracy of the aeroelastic simulation [1].

A coupled fluid-structure analysis alleviates these limitations while minimizing interpolation errors due to the data transfer. It also has the advantage of predicting the unsteady aerodynamics and the vibratory stresses in a single simulation, thus simplifying the HCF analysis process considerably (Fig. 1). The same finite element model is used for the fluid and the structure, thereby obviating the need for data transfer algorithms and removing the often introduced simplification that the motion of the structure be a combination of the structural modes. Thus, it better captures the inherently nonlinear coupling between the fluid and the structure, allowing more accurate predictions of the vibratory stresses responsible for HCF.

The coupled fluid-structure analysis TAM-ALE3D is a 3-D finite element solver with multimaterial capability. Its arbitrary Lagrangian Eulerian (ALE) solver makes it suitable for the simulation of the fluid-structure interaction between the airfoil and the flow exciting it. The ALE formulation treats the fluid-structure system as one continuum and the problem is formulated such that the governing equations are discretized in a unified fashion and then integrated simultaneously in time. This approach combining the best features of both Lagrangian and Eulerian methods was first introduced by Hirt et al. [2] for fluid flows at all speeds. Since then, it has come to be used widely for transient, high-speed large deformation problems of solids [3]. Donea [4] used the ALE formulation to model fluid-structure interaction because the freedom of moving the mesh in this formulation was advantageous for treating relative sliding at the fluid-structure interface. Bendikson [5] used this approach for flutter calculations and demonstrated that it minimized errors in energy transfer between the fluid and the structure.

By modeling the fluid and the structural domains using the same finite element method, the ALE formulation in TAM-ALE3D allows a seamless coupling between the two. However, the original version of the solver was restricted to Euler and laminar viscous calculations and was therefore only able to address blade vibration due to potential/shock forcing functions [6].

However, turbulent airfoil wakes are the primary forcing function resulting in HCF. Thus, to predict the response of blade rows to wake forcing functions, TAM-ALE3D must be extended to model turbulent wakes. This is accomplished herein by incorporating the Baldwin–Lomax turbulence model into the flow solver. This turbulent viscous model is then utilized to simulate the unsteady aerodynamic interactions in the Purdue High Speed Compressor at

Presented as Paper 0193 at the AIAA Aerospace Sciences Meeting, Reno, Nevada, 5–8 January 2004; received 15 April 2005; revision received 22 June 2006; accepted for publication 4 May 2006.

*Graduate Research Assistant, Student Member AIAA. Currently at GE Global Research Center, Niskayuna, New York.
†Associate Professor, Member AIAA.
‡McAllister Distinguished Professor, Fellow AIAA.

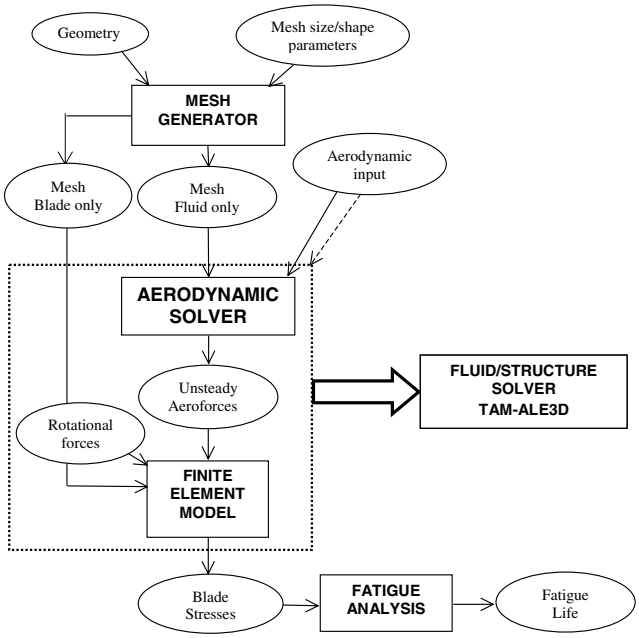

Fig. 1 HCF prediction systems.

the part-speed condition at which detailed experimental data are available [7,8]. The resonant response of the stator vanes to the unsteady aerodynamic excitation at the third vane resonant frequency is then predicted.

Mathematical Model

The mass, momentum, and energy equations are marched forward in time, with the physical domain discretized by an assembly of hexahedral elements. These elements are not required to move with the material as in a Lagrangian calculation nor remain fixed in space as in an Eulerian method. Rather they are allowed to move independent of the continuum, making the scheme an ALE scheme.

The governing equations are written with respect to a reference frame moving with an arbitrary velocity. The mass, momentum, and energy conservation equations for a control volume V of the continuum enclosed by the surface $S(x_i, t) = 0$ are

$$\frac{\partial}{\partial t}\int_V \rho \,\mathrm{d}V + \int_S \rho(u_i - U_i)n_i \,\mathrm{d}S = 0 \tag{1}$$

$$\frac{\partial}{\partial t}\int_V \rho u_i \,\mathrm{d}V + \int_S \rho u_i(u_i - U_i)n_i \,\mathrm{d}S = \int_S (n_j\sigma_{ij} - qn_i)\,\mathrm{d}S + \int_V \rho b_i \,\mathrm{d}V \tag{2}$$

$$\frac{\partial}{\partial t}\int_V \rho E \,\mathrm{d}V + \int_S \rho E(u_i - U_i)n_i \,\mathrm{d}S = \int_V (\sigma_{ij}u_{i,j} - qu_{i,i})\,\mathrm{d}V + \int_V \frac{\partial}{\partial x_i}\left(\kappa\frac{\partial T}{\partial x_i}\right)\mathrm{d}V \tag{3}$$

where u_i denotes the material velocity, $U_i = \partial x_i/\partial t$ is the grid velocity, x_i is the position vector of any point on the surface of the control volume, σ_{ij} is the stress tensor (symmetric), and the q term is the shock viscosity. The shock viscosity is a numerical device to smear out shocks to distances comparable to the mesh spacing so that a fine mesh is not required in the vicinity of the shock. It is represented by a quadratic plus linear form [9]:

$$q = \begin{cases} -C_0\rho\ell^2|u_{i,i}|u_{i,i} - C_1\ell\rho A u_{i,i} & \text{if } u_{i,i} < 0 \\ 0 & \text{if } u_{i,i} \geq 0 \end{cases} \tag{4}$$

with ℓ a length on the order of the mesh interval, A the speed of sound, C_0 the quadratic q coefficient ($\sim$1), and C_1 the linear q coefficient ($\sim$0.1).

Equations (1–3) are solved by an operator splitting technique. For each step forward in time, there are three distinct substeps: 1) the Lagrange step, 2) the mesh relaxation step, and 3) the advection step. In the Lagrange step, the velocity of the reference frame is set equal to the fluid velocity and it is allowed to move with the fluid. At the end of the Lagrange step, the mesh is moved to an arbitrary position to relieve the mesh distortion (mesh relaxation step). The system is now frozen in time and the fluid variables at the new mesh positions are recalculated by means of an advection calculation. At the end of the advection step, the time step for the next iteration is calculated and the solution proceeds to the next time step.

Discretization Procedure

A finite element method is used to discretize the equations. Spatial discretization is accomplished by a mesh of linear hexahedral elements. Physical quantities are assigned to staggered locations in the finite element. Velocities and accelerations are stored at the element nodes and vary trilinearly over the element. The element pressure, energy, and q term are stored at the element center and are constant over the element. Mass is stored at both the element center and the element nodes, with the nodal mass being one-eighth the sum of the surrounding element masses.

In the temporal discretization, the velocities and the q terms are calculated at half times, denoted by the superscript $n \pm 1/2$, with all other quantities evaluated at full times. This staggering of dependent variables is a compact way of achieving equations that are centered in space and time and are thus second order accurate [9].

Lagrange Step

In the Lagrange step, the mesh moves with the fluid. The convective terms in the governing equations thus drop out and the time derivative is recognized as the material derivative. The nodal accelerations a_i^n at time t^n are now calculated from the discretized momentum equation

$$\left(M' a_i^n\right)_\alpha = \sum_e \left[n_j'\left(\sigma_{ij}^n\right)_e - (q^{n-1/2})_e n_i'\right]\Delta S' + \left(M' b_i^n\right) + F_{i\alpha}^{\mathrm{hg}} \tag{5}$$

where the superscript on the right-hand side denotes the time level; the subscripts α and e denote node and element. The summation is over all nodes with node α in common, that is, eight elements for an interior node, or four, two, or one element for a boundary node. M' is the nodal mass, $\Delta S'$ is 1/4 of the area of each face of each element to which node α is common, n' is the unit normal to that face, and $F_{i\alpha}^{\mathrm{hg}}$ is the hourglass resisting force applied on each node to control the growth of hourglass modes of deformation.

For a reference frame rotating at a constant angular velocity ω_i, the body force per unit mass b_i^n includes both Coriolis and centripetal accelerations,

$$b_i^n = -2\varepsilon_{ijk}\omega_j u_k^{n-1/2} - \varepsilon_{ijk}\omega_j\left(\varepsilon_{klm}\omega_1 r_m^n\right) \tag{6}$$

where r_m^n is the position vector at time n, and ε_{ijk} is the alternating unit tensor.

After calculating the nodal acceleration from Eq. (5), centered differences are used to find the velocity at time $n + 1/2$. Centered differences are again applied to the velocity to find the new position of the node at time $n + 1$.

$$u_i^{n+1/2} = u_i^{n-1/2} + \Delta t^{n+1/2} a_i^n \tag{7}$$

$$x_i^{n+1} = x_i^n + \Delta t^n u_i^{n+1/2} \tag{8}$$

where Δt^n is the time step from n to $n + 1$, with $\Delta t^{n+1/2} = 0.5(\Delta t^n + \Delta t^{n+1})$.

Note that in general $\Delta t^n \neq \Delta t^{n+1/2}$ because the time step is allowed to vary during the simulation. However, with multiple blade rows, the time step is fixed to avoid interpolation in time when information is passed between the blade rows. This time step Δt is chosen small enough to satisfy the restrictions arising from the Lagrange and advection steps in all domains. Once the updated velocity and displacement fields are known, the stress tensor at the new time level is calculated using the appropriate constitutive equation. A linear elastic constitutive model is used for the solid and the fluid is taken to be Newtonian.

The Lagrange step is completed using conservation of energy to update the elemental energy. The Lagrangian energy equation is obtained by setting $U_i = u_i$ in Eq. (3),

$$\frac{D}{Dt}\int_V \rho E \, \mathrm{d}V = \int_V (\sigma_{ij} u_{i,j} - q u_{i,i}) \, \mathrm{d}V + \int_V \frac{\partial}{\partial x_i}\left(\kappa \frac{\partial T}{\partial x_i}\right) \mathrm{d}V \quad (9)$$

Integrating Eq. (9) with constant stress elements using $\sigma_{ij} = P\delta_{ij} + S_{ij}$, and noting that the inner product of a symmetric and antisymmetric tensor is zero yields

$$\frac{D}{Dt}(\rho E V) = S_{ij}\bar{D}_{i,j}V - (P+q)\frac{DV}{Dt} + H \quad (10)$$

where P is the pressure (thermodynamic pressure for the fluid and mechanical pressure for the solid), $\bar{D}_{ij}$ is the element mean value of the strain rate tensor, and H is the element internal energy increase by heat conduction,

$$H = \int_V \frac{\partial}{\partial x_i}\left(\kappa \frac{\partial T}{\partial x_i}\right) \mathrm{d}V = \int_S \left(\kappa \frac{\partial T}{\partial x_i}\right) \cdot \hat{n} \, \mathrm{d}S \quad (11)$$

Because the temperature T is cell centered, a finite volume rather than a finite element type discretization is used to compute H. The heat conduction term is calculated only for the fluid because the thermal response of the solid is not of interest.

For the solid, Eq. (10) is integrated using central differencing in time, whereas a third order Runge–Kutta method is used for the fluid. At the end of the integration, the pressures for the solid and the fluid are updated using appropriate equations of state.

Turbulence Modeling

The Baldwin–Lomax [10] model is a two-layer model with separate equations for the eddy viscosity in the inner and the outer layers and a smooth transition between the two different formulations. It is chosen because it is a standard model that is easy to implement in the TAM-ALE3D framework. The eddy viscosity is given by

$$\mu_t = \begin{cases} (\mu_t)_{\text{inner}}, & y \leq y_{\text{crossover}} \\ (\mu_t)_{\text{outer}} & y > y_{\text{crossover}} \end{cases} \quad (12)$$

where y is the normal distance to the nearest wall, $y_{\text{crossover}}$ is the smallest y value at which the viscosities from the inner and the outer formulations are equal, and,

$$(\mu_t)_{\text{inner}} = \rho \ell^2 |\omega| \qquad (\mu_t)_{\text{outer}} = K C_{\text{cp}} \rho F_{\text{wake}} F_{\text{Kleb}}(y) \quad (13)$$

$\ell = \kappa y(1 - e^{(y^+/A^+)})$ is the mixing length multiplied by the Van Driest damping factor, and the normal distance in wall coordinates is

$$y^+ = y(\sqrt{\rho|\omega|/\mu_{\text{lam}}})_{\text{wall}} \quad (14)$$

The variable $F_{\text{wake}} = y_{\max} F_{\max}$ where $y_{\max}$ and $F_{\max}$ are determined from the function

$$F(y) = y|\omega|[1 - e^{(y^+/A^+)}] \quad (15)$$

with $F_{\max}$ being the maximum $F(y)$ across the boundary layer, and $y_{\max}$ the normal distance y corresponding to $F_{\max}$. $F_{\text{Kleb}}(y)$ is the Klebanoff intermittency function

$$F_{\text{Kleb}}(y) = [1 + 5.5(C_{\text{Kleb}} y / y_{\max})^6]^{-1} \quad (16)$$

The turbulence model is implemented in an unstructured fashion, able to accommodate moving grids. Boundary layer calculations are carried out in the wall normal direction and wake calculations across the entire wake. Inside the boundary layer, both the inner and the outer formulations are used to determine the eddy viscosity, whereas only the outer formulation is used for wakes because there is no wall shear stress. Note that for wakes, y refers to the distance from the wake centerline which is calculated frequently during the simulation. To limit spuriously high values, the turbulent viscosity is limited to 1000 times the laminar value [11]. The turbulent viscosity thus calculated is added to the laminar viscosity to obtain the total viscosity used to calculate the shear stress from the Newtonian constitutive equation.

Mesh Relaxation

In the Lagrange calculation, the mesh moves with the continuum. Clearly, the fluid elements cannot continue to move in a Lagrangian fashion because element locking will occur due to large shear deformation. Therefore, before proceeding to the next time step it is necessary to move the fluid mesh to a new position and recalculate the elemental and nodal quantities by an advection calculation. This process of moving the mesh to a new position is called mesh relaxation. The structural mesh is not relaxed because the solid can be modeled from a Lagrangian perspective throughout the simulation.

For the fluid mesh, it is critical to maintain good resolution near the airfoil surface to resolve the boundary layer. A spring analogy is used to move the fluid nodes to their new positions [12,13], with the mesh replaced by an array of fictitious springs and acting like an elastic medium. The equilibrium position of this mesh is taken to be the pre-Lagrange position, and any mesh motion during the Lagrange step is considered to be a distortion imposed on the mesh/spring system. Consequently, during the mesh relaxation step, this distortion is relieved by moving the mesh to a new position given by

$$\boldsymbol{\delta}_i^{n+1} = \sum_{j=1}^{N} \alpha_{ij} \boldsymbol{\delta}_j^n \Big/ \sum_{j=1}^{N} \alpha_{ij} \quad (17)$$

where $\boldsymbol{\delta}_i^n$ refers to the displacement of node i from the pre-Lagrange position, n refers to the iteration number or the number of smoothing operations, and N is the number of nodes attached to node i.α_{ij} is the stiffness of the leg connecting nodes i and j given by

$$\alpha_{ij} = \phi[(x_i - x_j)^2 + (y_i - y_j)^2 + (z_i - z_j)^2]^{\psi} \quad (18)$$

with ϕ and ψ user defined parameters to vary the stiffness of the springs.

By increasing the stiffness of the springs near the boundary, better resolution can be attained over the surface of the airfoil. Only the nodes close to the airfoil surface are moved according to Eq. (17), the rest are put back to their pre-Lagrange positions. Thus, the grid relaxation method serves to locally diffuse the mesh distortion at the airfoil surface boundary while maintaining the initial configuration of the mesh.

Advection

As a fluid element moves from its position at the end of the Lagrange calculation to its new position after mesh relaxation, there is mass, momentum, and energy flux through the six faces of the element. The advection calculation is not performed for the solid because it is modeled from a Lagrangian perspective throughout the simulation.

Because advection is merely a geometric update of the mesh, the source terms on the right-hand side of the governing equations disappear. The new mass, momentum, and energy of the element are obtained by summing the flux of these quantities through the element faces. Consider a single face of an element that moves from its old

position to a new position after mesh relaxation. The volume between the old and the new face positions is called the face-swept volume ΔV_f. The change in mass, momentum, and energy of the element are

$$\Delta M_e = -\sum_{k=1}^{6} (\rho^* \Delta V_f)_k \tag{19}$$

$$\Delta (M' u_i)_\alpha = -\sum_{k'=1}^{6} [(\rho u_i)^* \Delta V_f]_{k'} \tag{20}$$

$$\Delta (ME)_e = -\sum_{k=1}^{6} [(\rho E)^* \Delta V_f]_k \tag{21}$$

where the summation is over the element's six faces.

Note that because momentum is stored at the nodes, momentum advection is performed with a "node-centered" element whose center is the node under consideration and corners, the centers of the surrounding elements. Also, the starred quantities are the values at the center of the face-swept volume, determined by a second-order upwinding scheme which requires information from the two elements upwind of the face and one downwind element. Monotonic limiters are used to ensure that these quantities are always bounded by the corresponding quantities in the upwind and downwind elements.

Boundary Conditions

Airfoil Surface Boundary

The no slip boundary condition is required at the airfoil surface. In addition, momentum and energy must be exchanged between the airfoil and the flow at the interface. This is accomplished by requiring the fluid and the airfoil nodes on this boundary to move as a single body during the Lagrange acceleration calculation. Interpolation routines allow for the fluid and airfoil nodes to be noncontiguous.

During the Lagrange or advection calculation, the fluid nodes could move away from the airfoil surface. Therefore, at the end of both these calculations, the fluid nodes on the airfoil are projected back on to the airfoil surface thereby maintaining geometric continuity at the airfoil surface. In addition, the velocities of these nodes are set to zero with respect to the airfoil. The fluid nodes at the blade trailing edge are allowed to move freely during the Lagrange calculation. However, after the advection calculation their velocities are set to zero with respect to the airfoil.

Periodic Boundaries

Only one blade passage is analyzed for each blade row, with the flow variables transferred directly between adjacent airfoil passage boundaries. This corresponds to a 0 deg interblade phase angle.

Hub and Tip Boundaries

The cylindrical surfaces at the hub and tip are treated as slip surfaces, with the airfoils extending from hub to tip. To enforce the boundary condition, the fluid nodes next to the hub and tip surfaces are projected normally onto these surfaces and the normal velocity component is set to zero at the end of both the Lagrange and the advection steps. However, the airfoil nodes on the hub and the tip are allowed to move and are not constrained to the hub/tip boundaries.

Inflow and Outflow Boundaries

For an axial subsonic flow, the velocity, density, and energy flux are specified at the inflow and static pressure at the outflow. During the Lagrange calculation, the exit static pressure is included in the force summation of Eq. (5) for those nodes on the outflow boundary. For the inflow, the velocities calculated by Eq. (7) are ignored and overwritten by the specified inflow velocity. For the advection step, the fluxes at the inflow need to be specified. The density and energy flux are explicitly specified, and the momentum flux is calculated from the specified inflow velocity.

To minimize reflections at the inflow and outflow boundaries, boundary conditions of the type described by Giles [14] are used. These allow acoustic waves normal to the inflow and outflow boundaries to pass out of the domain without reflection.

The inflow boundary is made partially nonreflecting by adding the following perturbations to the specified inflow quantities:

$$\Delta \rho^{\text{inflow}} = -\frac{\rho_{\text{avg}} \Delta u_1^{\text{ext}}}{2A_{\text{avg}}} + \frac{\Delta P^{\text{ext}}}{2A_{\text{avg}}^2} \tag{22}$$

$$\Delta u_1^{\text{inflow}} = \frac{\Delta u_1^{\text{ext}}}{2} + \frac{\Delta P^{\text{ext}}}{2\rho_{\text{avg}} A_{\text{avg}}} \tag{23}$$

$$\Delta (\rho E)^{\text{inflow}} = \frac{1}{(\gamma - 1)} \left[-\frac{\rho_{\text{avg}} A_{\text{avg}} \Delta u_1^{\text{ext}}}{2} + \frac{\Delta P^{\text{ext}}}{2} \right] \tag{24}$$

where the superscript "ext" indicates that this perturbation quantity is extrapolated from the interior, adjacent to the inflow boundary, the subscript "avg" denotes the time average, with this being the user-specified properties at inflow, and the velocity under consideration in this one-dimensional nonreflecting boundary condition being the axial velocity parallel to the engine centerline.

At the outflow boundary, the specified pressure is perturbed with

$$\Delta P^{\text{outflow}} = \frac{\rho_{\text{avg}} A_{\text{avg}} \Delta u_1^{\text{ext}}}{2} + \frac{\Delta P^{\text{ext}}}{2} \tag{25}$$

where the time-averaged outflow pressure is specified, but the other outflow time-averaged quantities are calculated as part of the solution.

Multidomain Computations

Parallel computations are performed by placing a segment from each blade row on a processor. Information passing between processors is accomplished with message passing interface (MPI) standard library calls. For blade rows with equal blade counts as in this study, this segment is a single blade passage, with periodic boundaries accounting for the complete blade row. To simplify the interpolation between upstream and downstream domains, there are equal numbers of element faces on the interface between domains equally spaced tangentially and radially.

In the Lagrange calculation, the nodal forces due to the element pressure, the q term, and the hourglass viscosity are first calculated without accounting for the presence of the other domain. These forces, as well as the nodal masses at the inflow boundary of the downstream domain, are then passed to the upstream domain. The two domains are offset due to rotation, so interpolation is performed and the forces and masses added to the upstream outflow boundary nodal forces and masses. The net nodal acceleration is calculated by dividing the net nodal force by the net nodal mass. These accelerations are passed to the downstream domain and interpolated to the downstream nodal locations. Finally, Coriolis and centripetal accelerations b_i^n are added.

For the advection of mass and energy, second-order accuracy is maintained at the interface between domains. The momentum advection calculation at the outflow boundary of the upstream domain is performed without information from the downstream domain, that is, the interface is treated as an outflow boundary. The computed velocities are then passed to the inflow boundary of the downstream domain. These velocities are interpolated to the downstream nodal positions and then transformed to account for the relative rotation between domains.

Results

A viscous TAM-ALE3D coupled fluid-structure simulation of the Purdue Transonic Compressor stator vane resonant response driven

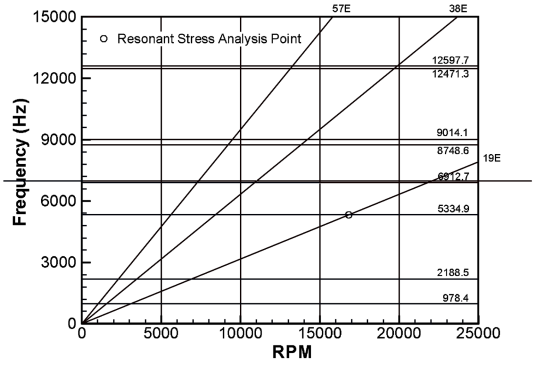

Fig. 2 Stator vane Campbell diagram.

by the upstream rotor wakes is performed. The compressor is a $1\frac{1}{2}$ stage axial-flow geometry representative of that used in the front stages of aircraft engine high-pressure compressor designs. It has a constant hub-tip ratio of 0.667 and a tip diameter of 0.3 m. The inlet guide vane (IGV) and stator rows have 18 vanes and the rotor has 19 blades, with only the rotor stator modeled in this simulation. The stator profile is an advanced controlled diffusion airfoil design with a 4.45 cm chord and a constant 7% thickness. The rotor blades have a NACA 65 series profile on circular arc mean lines with a 5.08 cm chord and a thickness distribution varying from 10% at the hub to 6% at the tip.

Of particular interest to this study is the part-speed operating condition. Experiment and modal analyses using finite element solvers show that the stator vane third natural mode is excited by the upstream rotor wakes near the part-speed operating point as seen in the stator vane Campbell diagram, Fig. 2. To investigate this operating point, the viscous analysis is first experimentally validated by simulating the rotor-stator interaction unsteady aerodynamics and comparing with the data obtained with the instrumented stator passage shown in Fig. 3.

A TAM-ALE3D coupled fluid-structure simulation of the resonant response of the stator vanes to the rotor wakes is then performed. Note that in these simulations, the number of stator vanes is changed to 19 so that single blade passages can be used to simulate both rotor and stator rows corresponding to an interblade phase angle of zero. This does not change the rotor blade pass period (BPP), with the rotor and stator blade rows assigned to different processors using MPI.

Rotor-Stator Aerodynamic Interactions

The rotor passage is modeled with 37,770 hexahedral elements and the stator passage with 41,040 elements. The airfoils are modeled with shells and are held fixed during this simulation. The rotor passage uses a *C* grid wrapped around the blade surrounded by *H* grids, with a total of 52 points in the axial direction and 49 points in the blade-to-blade direction. The stator passage is composed entirely of *H* grids, with 58 points axially and 49 points in the vane-to-vane direction. Both passages have 16 points in the spanwise direction and 16 points in the wall normal direction near the airfoils to resolve the boundary layers. In addition, the trailing edge of the rotor blade and the leading and trailing edges of the stators have been modified into wedges. The smallest value of the near wall mesh spacing is about $y^+ = 1$ for the rotor and $y^+ = 0.2$ for the stator passage mesh.

The inflow conditions are obtained from the inviscid IGV-rotor simulation of the Purdue Transonic Compressor at the same operating condition. The solution is marched in time with a time step of 0.04 μs (5263 time steps/period) until a periodic steady state is reached and total pressure ratio matches the measured value. This convergence to the periodic steady state takes about 8 ms and approximately 220 h of CPU time on each of two processors of an IBM SP2.

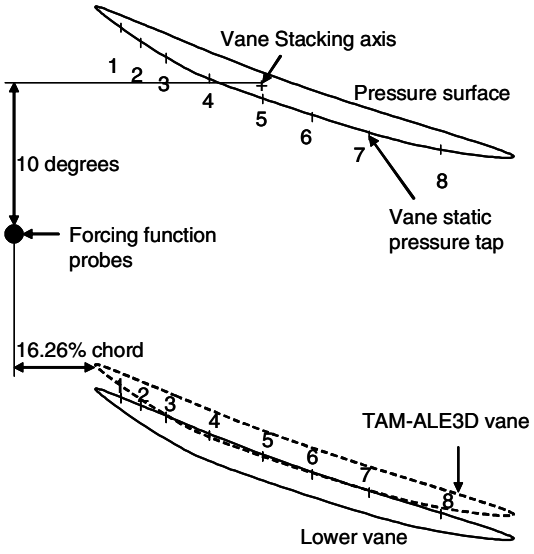

Fig. 3 Location of passage instrumentation.

Stator Unsteady Aerodynamics

Figure 4 shows the stator vane surface predicted and measured unsteady aerodynamic response at the times corresponding to the wake forcing function results shown in the figure center. Results from a coarser grid with 50% fewer elements are also included. The vane/blade initial position for the data corresponds to the rotor stacking axis being at the center of the reference passage at $t = 0$. Because the actual geometry features 18 stators and the simulation features 19, the simulation forcing function "probe" is placed 10 deg below the upper vane in the reference passage so that the phase lag between the forcing function and vane response is the same as the experiment. Therefore, the flow angle measurements at the probe

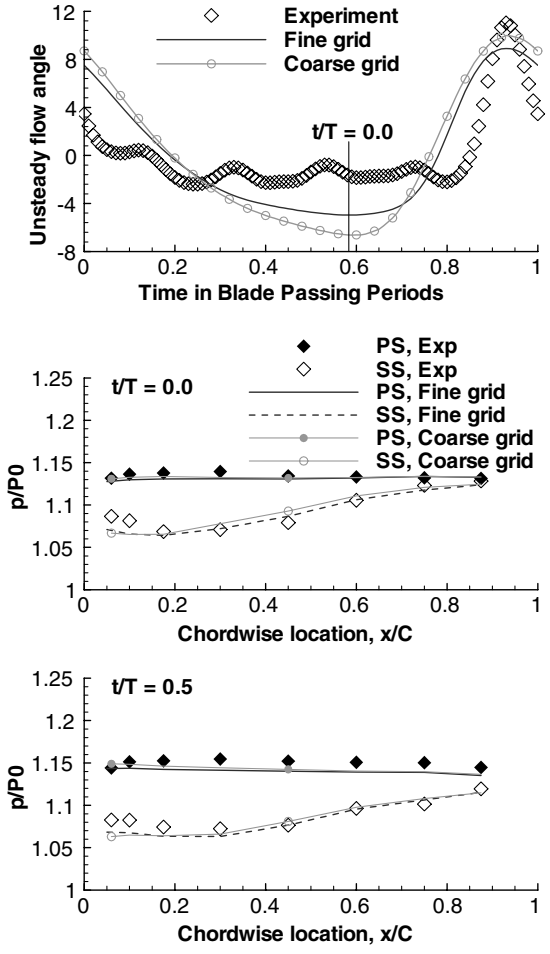

Fig. 4 Instantaneous stator surface pressures at midspan.

location lag the unsteady pressures on the vane by 10 deg, that is, 0.585 times the rotor blade pass period, shown by vertical lines on the forcing function plot, that is, the vertical line represents the unsteady flow angle upstream of the vane at the instances the vane response is measured. The forcing function is represented in terms of the variation in the absolute flow angle which is related to the stator incidence and is also an indicator of the rotor wake characteristics.

The simulation overpredicts the mass-averaged mean flow angle by 3 deg as well as the breadth and depth of the rotor wake. Grid resolution studies show that this is primarily because of the coarse grids used. However, the predicted instantaneous stator surface pressures exhibit very good correlation with data. Note that the stagnation pressure at the compressor inlet is used to normalize the instantaneous pressures. The suction and pressure surface pressure fluctuations are approximately 180 deg out of phase [8], with this phase shift very prominent near the leading edge, as expected.

Figure 5 shows the stator midspan steady and unsteady lift per unit span. The computed steady lift is within 5% of the data, with the slight loading underprediction over the aft 70% of the chord responsible for this difference. The unsteady lift results show that the predicted and measured amplitudes agree reasonably well for both grids, with the rms error in the unsteady lift predictions being 8.8 and 9.4 N/m, respectively, for the fine and coarse grids. As the unsteady results are time shifted to provide the best match between the experimental and computed forcing functions, the good agreement in the unsteady lift phase implies that the phase lag between the forcing function and the predicted unsteady lift is in good agreement with the data.

This prediction of the stator surface unsteady pressures and unsteady lift, that is, the driving force for the flow-induced vibrations of the stator, demonstrates that this simulation is suitable for the prediction of the resulting vibratory stress.

Wake Chopping and Transport

The rotor blade wakes are periodically chopped by the stator vanes and transported through the stator passage. Because the rotor wakes have an excess tangential velocity over the freestream fluid in the stator frame of reference, chopping of the rotor wakes by the stators leads to incidence changes, causing unsteady loading on the stator.

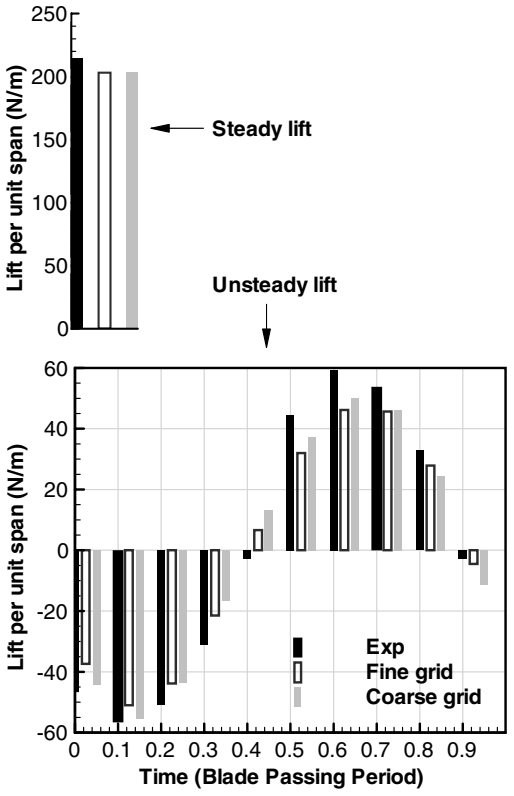

Fig. 5 Lift/span on stator vane at midspan.

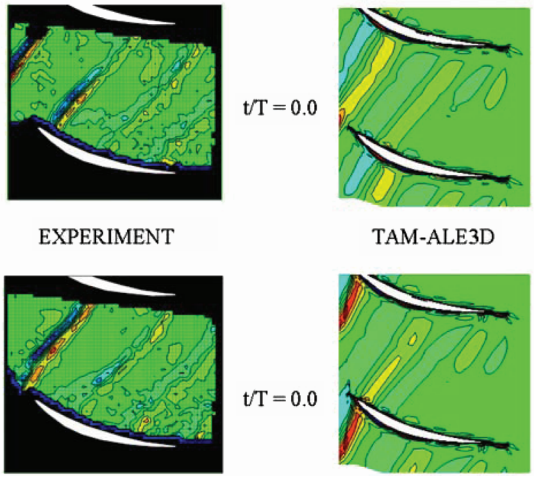

Fig. 6 Stator passage flowfield at midspan: data are ensemble averaged, computed values unsteady.

Another unsteady flow phenomenon occurs as the rotor wakes are chopped and transported through the downstream stator passages: the drift and accumulation of the wake fluid on the pressure surface of the stators. This occurs because the rotor wakes have a tangential slip velocity relative to the freestream in the stator frame. Figure 6 presents time instances of computed unsteady vorticity from the fine grid and compares them to ensemble-averaged vorticity data at two instants in a rotor blade pass period. The contour levels for the experimental and computed results presented in Fig. 6 are different; the figure serves to show that the qualitative nature of the wake chopping and transport is captured by the solver.

Thus, TAM-ALE3D is able to predict the mechanics of the wake chopping and transport process which are responsible for the unsteady loading on the vanes. In addition, the surface pressure distributions and the temporal phase of the unsteady loading at midspan are captured well.

Stator Vane Modal Analysis

The structural dynamic capabilities of TAM-ALE3D are validated by extracting the modal properties of the stator vane. The TAM-ALE3D finite element model of the steel stator vane is a mesh having 3375 nodes and 2464 hexahedral elements, Fig. 7. Four elements are used across the thickness and 14 elements across the span. At the tip, nodes between 15 and 60% chord are fixed. These nodes are on the

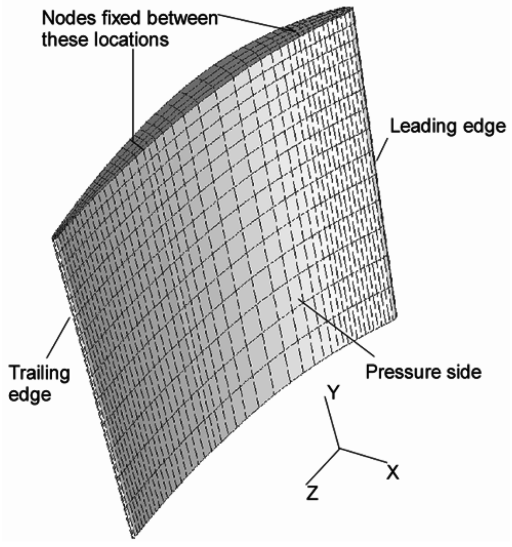

Fig. 7 Stator vane mesh.

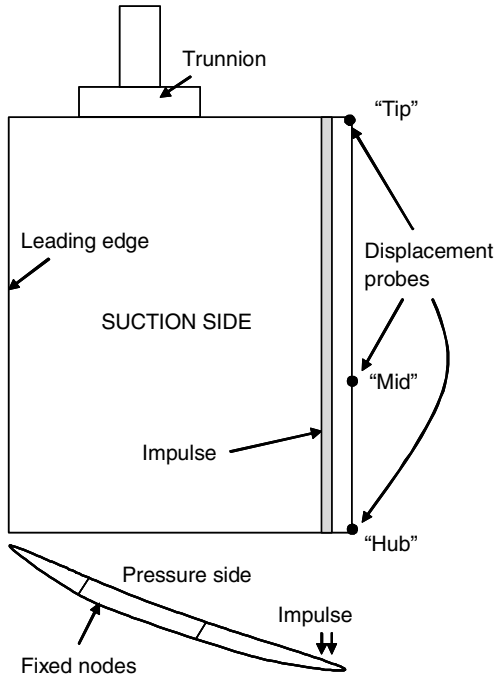

Fig. 8 Impulse test displacement probe locations.

joint between the trunnion and the vane. TAM-ALE3D does not model the trunnion which is fixed to the case; hence the nodes on the joint are fixed.

Because TAM-ALE3D does not perform a modal analysis, the modal parameters cannot be determined directly. They can, however, be calculated by an impulse test of the stator vane in vacuum. An impulse is applied near the trailing edge on the pressure side of the vane, as shown in Fig. 8. The impulse is such that it is uniform in magnitude between the points marked "tip" and "mid," and again between mid and "hub" but with a different magnitude and sign. The stator third mode involves trailing edge twisting motion along the span [15] with a node near the point marked mid. Thus, the impulse which is applied for 200 μs at the start of the simulation is designed primarily to excite the third mode.

After the start of the simulation, the vane response is recorded for a period of 20 ms. The normal displacement of the three points noted and the entire suction surface of the vane are recorded. The displacement time histories of these different points on the vane are used to determine the modal parameters.

Figure 9 shows the normal displacement time history at the two trailing edge nodes. The tip displacement is relatively small compared to that at the hub. Note that the displacements of these points decay in time. This is due to the hourglass viscosity which is used to prevent the growth of hourglass modes of deformation in the finite element solution. The hourglass viscosity functions as an apparent structural damping and serves to limit the vibration.

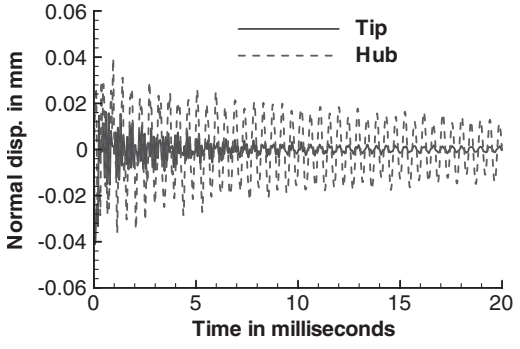

Fig. 9 Hub and tip displacement probe response.

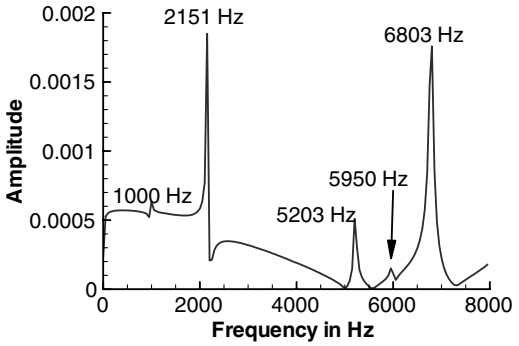

Fig. 10 Tip displacement frequency spectrum.

The frequency spectrum shown in Fig. 10 is obtained by a Fourier decomposition of the tip displacement. The first five natural modes are excited by the impulse, with the participation from modes two and five being the largest. The third mode with a natural frequency of 5203 Hz is of interest because with 19 rotor blades, an excitation at this frequency corresponds to a rotor rpm of 16,430 rpm which is near the part-speed operating condition of 15,000 rpm. Natural frequency results obtained from a simulation with a more refined grid of 5635 nodes are almost identical, with both comparing well with data [15], Table 1.

To obtain the mode shapes, the normal displacements of all points on the suction surface are Fourier transformed. The imaginary part of the discrete Fourier transform (DFT) coefficient can be used as an indicator of both the relative magnitude and phase of the response of any point on the vane. The peaks of the imaginary part of the DFT corresponding to the third mode are then picked off for each point, scaled, and plotted against the undeformed suction surface coordinates, Fig. 11. As seen, the TAM-ALE3D mode shape determined by this peak-picking approach matches the measured holographic mode shape well.

In summary, TAM-ALE3D predicts the unsteady aerodynamics at midspan and the vane structural dynamics quite well.

Stator Vane Vibratory Stress

A coupled TAM-ALE3D fluid-structure interaction simulation of the stator at the third mode resonance rpm is now performed. The stator vane structural grid is the same as the one used to determine the natural frequencies and mode shape. The rotor blade is also modeled with bricks but its response is not of interest. The rotor and stator passages are modeled with approximately 27,000 and 28,000 elements, respectively, with 15 elements each in the spanwise direction. The topology of these fluid-structure meshes is the same as the aerodynamic meshes described earlier. A midspan slice of the rotor and stator meshes is shown in Fig. 12.

The computational procedure is as follows. The stator vanes are not allowed to respond while the periodically unsteady flow due to the rotation of the upstream rotor is established. The rotor speed is 16,430 rpm which corresponds to an exciting frequency of 5203 Hz. A periodic steady state is reached in 6 ms or 31 rotor BPPs, consuming 80 h of CPU time on each of two processors running in parallel on an IBM SP2. The steady "operating point" of the simulation is characterized by a total pressure ratio of 1.23 and a mass flow rate of 10.05 lb_m/s. Because the stator vanes are not allowed to vibrate, a large time step of 0.05 μs (3844 time steps/period) is used for this aerodynamics-only simulation.

Table 1 Natural frequencies (Hz) of stator vane

Mode	1	2	3	4
Medium grid	1000	2151	5203	5950
Fine grid	1000	2150	5250	5998
Holography	980	2192	5334	5968

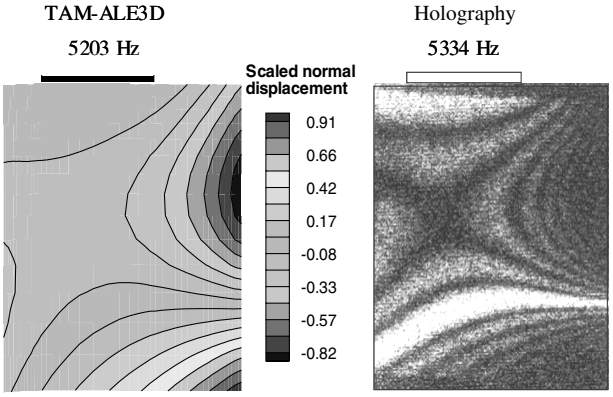

Fig. 11 Predicted and measured stator mode 3.

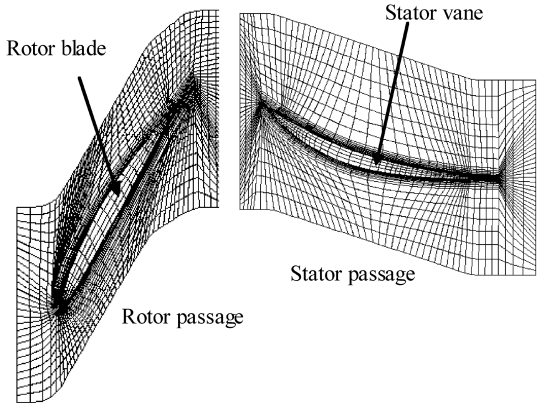

Fig. 12 Midspan rotor and stator passage meshes for fluid-structure simulation.

After the aerodynamics has reached a periodic steady state, the vanes are allowed to move freely in response to the flow. The time step is then reduced to 0.015 μs (12,813 time steps/period of structural vibration), being constrained by the speed of sound in the vane. The aerodynamics and the vane response are simulated for approximately 19 ms or 99 BPPs, which requires approximately 700 h of CPU time on each of two processors on an IBM SP2. Displacement and stress histories at various points on the stator vane, Fig. 13, are recorded over the duration of the simulation, with this response providing the amplitude of the stress intensities in the stator vane.

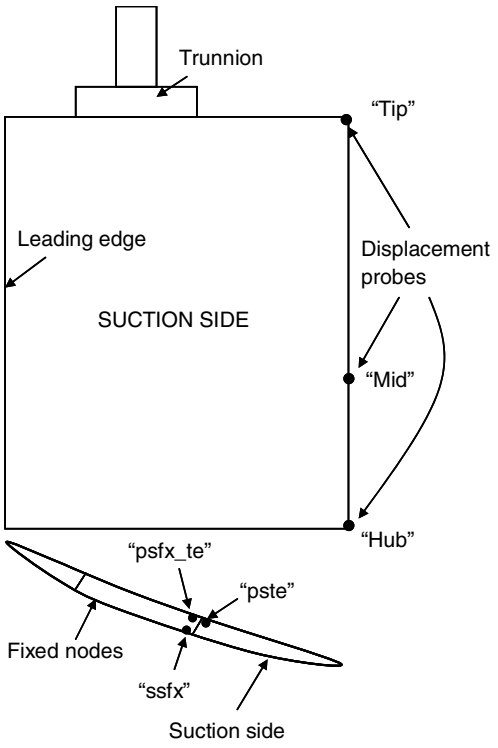

Fig. 13 Fluid-structure simulation probe locations.

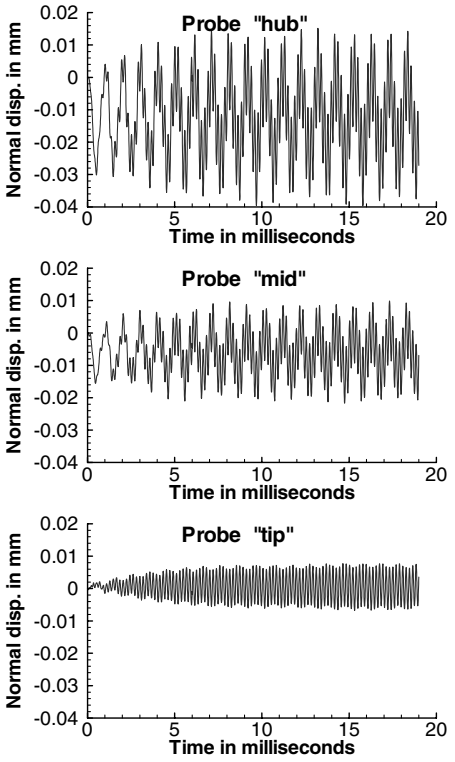

Fig. 14 Normal displacement time histories.

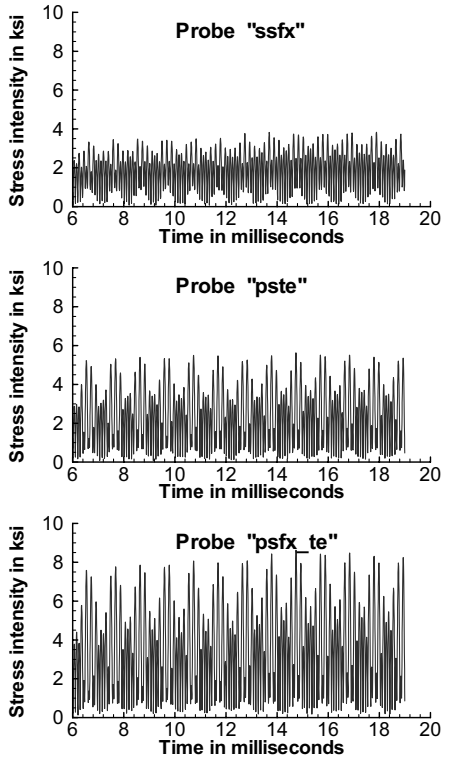

Fig. 15 Stress intensity amplitudes.

Figure 14 shows the normal displacement time histories recorded over the duration of the simulation by the displacement probes placed near the trailing edge. Note that the midprobe location for the fluid-structure simulation is not the same as the in-vacuum simulation. The maximum normal displacement of 0.04 mm occurs near the hub, with the displacement at the tip 5 times smaller. The frequency content of the displacement at these locations is quite different. The tip shows a predominantly higher frequency response, whereas the hub and midlocations have some contribution from the lower modes. DFTs of the hub and mid-displacements with different signal lengths show that the contribution from the lower modes decays with time, and is therefore a transient response.

Figure 15 shows the stress intensity amplitude time histories recorded at three different points on the vane over the last 13 ms of the simulation. The elements at the simulation stress probe locations experience both tensile and shear stresses. Hence the stresses are characterized by the maximum stress intensity amplitude calculated from the principal stresses as

$$\sigma_{\text{int}} = \max(|\sigma_1 - \sigma_2|, |\sigma_2 - \sigma_3|, |\sigma_3 - \sigma_1|) \tag{26}$$

where σ_1, σ_2, and σ_3 are the principal stresses.

Because the vane is cantilevered at the trunnion, the maximum stress intensity levels are observed under the pressure side trunnion joint towards the trailing edge, location "psfx_te" in Fig. 13. The predicted maximum total stress intensity level is approximately 8.5 ksi, with the contribution from the resonant frequency being approximately 3 ksi. For a stator vane which has much more mechanical damping than a rotor blade, and excited by thin wakes near the design point of the subsonic rotor, this level is in the range of expected vibratory stress.

Summary

HCF failure of turbomachine blades is a complex problem involving coupling between the unsteady flow and the resulting airfoil vibration. To obtain realistic estimates of vibratory stresses for HCF design, simulation tools must model coupled fluid-structure interaction in a multistage environment. In this study, such a unified fluid-structure interaction analysis, TAM-ALE3D, was developed and its HCF prediction capabilities demonstrated through correlations with data.

The unsteady viscous capabilities of TAM-ALE3D were validated by simulating the part-speed rotor-stator interaction in the Purdue Transonic Compressor for which benchmark experimental data are available. This is followed by a prediction of the modal properties of the stator vane. Both aerodynamic and structural predictions individually compare well with the corresponding data, validating the ability of TAM-ALE3D to correctly simulate unsteady aeroelastic phenomena in turbomachines. The resonant response of the stators generated by the upstream rotor blade wakes is then quantified by performing a viscous fluid-structure interaction simulation at the stator resonance condition, with the vane vibratory stresses predicted.

Acknowledgement

This research was sponsored, in part, by the Air Force Office of Scientific Research (AFOSR). This support is most gratefully acknowledged.

References

[1] Smith, M. J., Hodges, D. H., and Cesnik, C. E. S., "Evaluation of Computational Algorithms Suitable for Fluid-Structure Interactions," *Journal of Aircraft*, Vol. 37, No. 2, 2000, pp. 282–294.

[2] Hirt, C. W., Amsden, A. A., and Cook, J. L., "An Arbitrary Lagrangian-Eulerian Computing Method for All Flow Speeds," *Journal of Computational Physics*, Vol. 14, 1974, pp. 227–253.

[3] Benson, D. J., "Computational Methods in Lagrangian and Eulerian Hydrocodes," *Computer Methods in Applied Mechanics and Engineering*, Vol. 99, 1992, pp. 235–394.

[4] Donea, J., *Arbitrary Lagrangian-Eulerian Finite Element Methods*, edited by T. Belytschko and T. J. R. Hughes, Computational Methods for Transient Analysis, North-Holland, Amsterdam, 1983, pp. 473–516.

[5] Bendikson, O. O., "A New Approach to Computational Aeroelasticity," AIAA Paper 91-0939, April 1991.

[6] Gottfried, D. A., and Fleeter, S., "Turbomachine Blade Row Interaction Predictions with a Three-Dimensional Finite Element Method," *Journal of Propulsion and Power*, Vol. 18, No. 5, 2002, pp. 978–989.

[7] Sanders, A. J., Papalia, J., and Fleeter, S., "Multi-Blade Row Interactions in a Transonic Axial Compressor Part 1: Stator Particle Image Velocimetry (PIV) Investigation," *Journal of Turbomachinery*, Vol. 124, No. 1, 2002, pp. 10–18.

[8] Sanders, A. J., and Fleeter, S., "Multi-Blade Row Interactions in a Transonic Axial Compressor Part 2: Rotor Wake Forcing Function and Stator Unsteady Aerodynamic Response," ASME Paper 2001-GT-0269, July 2001.

[9] Noh, W. F., "Numerical Methods in Hydrodynamic Calculations," Lawrence Livermore National Laboratory, UCRL-52112, 1976, pp. 49–58.

[10] Baldwin, B. S., and Lomax, H., "Thin Layer Approximation and Algebraic Model for Separated Turbulence Flows," AIAA Paper 78-257, Jan. 1978.

[11] Turner, M. G., and Jennions, I. K., "An Investigation of Turbulence Modeling in Transonic Fans Including a Novel Implementation of an Implicit k-ε Turbulence Model," *Journal of Turbomachinery*, Vol. 115, No. 2, 1993, pp. 249–260.

[12] Batina, J. T., "Unsteady Euler Airfoil Solutions Using Unstructured Dynamic Meshes," *AIAA Journal*, Vol. 28, No. 8, 1990, pp. 1381–1388.

[13] Blom, F., and Leyland, P., "Analysis of Fluid-Structure Interaction on Moving Airfoils by Means of an Improved ALE Method," AIAA Paper 97-1770, 1997.

[14] Giles, M. B., "Nonreflecting Boundary Conditions for Euler Equation Calculations," *AIAA Journal*, Vol. 28, No. 12, 1990, pp. 2050–2058.

[15] Cross, C. J., "Turbomachine Airfoil Vibration Control Utilizing Active and Passive Piezoelectric Elements," Ph.D. Thesis, Purdue University, 1998.

F. Liu
Associate Editor